A backward-characteristics monotonicity preserving method for stiff transport problems

Ilham Asmouh[1][0009−0001−9930−9555] and Abdelouahed Ouardghi[2][0000−0003−3471−7424]

[1] Institut für Mathematik, Universität Innsbruck, Technikerstraße 13, 6020 Innsbruck, Austria
ilham.asmouh@uibk.ac.at
[2] Jülich Supercomputing Centre, Forschungszentrum Jülich GmbH, Germany
a.ouardghi@fz-juelich.de

Abstract. Convection-diffusion problems in highly convective flows can exhibit complicated features such as sharp shocks and shear layers which involve steep gradients in their solutions. As a consequence, developing an efficient computational solver to capture these flow features requires the adjustment of the local scale difference between convection and diffusion terms in the governing equations. In this study, we propose a monotonicity preserving backward characteristics scheme combined with a second-order BDF2-Petrov-Galerkin finite volume method to deal with the multiphysics nature of the problem. Unlike the conventional Eulerian techniques, the two-step backward differentiation procedure is applied along the characteristic curves to obtain a second-order accuracy. Numerical results are presented for several benchmark problems including sediment transport in coastal areas. The obtained results demonstrate the ability of the new algorithm to accurately maintain the shape of the computed solutions in the presence of sharp gradients and shocks.

Keywords: Flow transport · Backward characteristics method · Petrov-Galerkin finite volume method · Backward differentiation formula (BDF2).

1 Introduction

Convection-diffusion problems appear in various fields of science and technology such as heat and mass transfer, environmental protection, fluid dynamics and hydrology. These problems in highly convective flows are essentially characterized by some complicated features such as sharp shocks and shear layers which involve steep gradients in their numerical solutions. As a consequence, construction of efficient computational solvers to highly capture these flow features requires the adjustment of the local scale difference between convection and diffusion terms in the governing equations. Eulerian-based approaches have been widely used for the numerical solution of these problems. However, for convection-dominated cases, those methods exhibit spurious oscillations and numerical instabilities and stringent stability conditions are consequently unavoidable.

ICCS Camera Ready Version 2024
To cite this paper please use the final published version:
DOI: 10.1007/978-3-031-63783-4_4

Backward characteristics methods are among excellent integration schemes by the virtue of their stability properties and good accuracy. Indeed, By discretizing the Lagrangian derivative of the solution in time instead of the Eulerian derivative, we can exceed the maximum allowable time step while maintaining the efficiency of symmetric solvers. However, these methods can experience some difficulties preserving the shape and mass conservation of advected quantities. Several remedies have been proposed including addition of filters to impose monotonicity or positivity in the field of plasma physics [2]. However, this technique is challenging especially in higher order reconstruction due to the necessity of some conditions on the polynomials to be monotone or positive [3]. Weighted essentially non-oscillatory (WENO) reconstructions have been very popular [12, 14] even though these techniques are not convenient for long term simulation since they are known to be too dissipative. In this work, we propose combining low and high order interpolation schemes such that the interpolated value remains within the largest and the smallest values of the solution in a set of points surrounding the feet of the characteristics.

To deal with the diffusive terms, we propose a finite volume scheme. It is known that finite volume methods are very popular for their ability in capturing shocks, producing simple stencils and effectively treating Neumann boundary conditions and nonuniform grids, which make them an attractive choice for fluid flow simulation. However, finite volume schemes confront some challenges, in geneal, related to the accuracy of fluxes approximation which has an immediate impact on truncation errors if the fluxes are not approximated carefully. In contrast, the fluxes in finite volume element (FVE) methods are approximated by replacing the unknowns with a finite element solution. Thus, the best choice of finite element space makes the discretization design process bringing the focus to the local character of the solution rather than the equation. Furthermore, very effective discretization processes are provided for multilevel adaptive methods. Moreover, finite volume element methods are known as one of the preferred approaches as the test space essentially maintains the local conservation of the method without serious restrictions in terms of implementation. The method consists on a volume integral formulation of the problem using a finite partitioning set of volumes for the equation discretization and restriction of admissible functions to a finite element space for the solution discretization.

Several efforts have been investigated in this area. The authors in [5] analyzed some error estimates for finite volume finite element method for nonlinear convection-diffusion problems where nonlinear convective terms are approximated using a monotone vertex-centered finite volume scheme. In [4], the authors analyzed the stability of finite volume element scheme for parabolic problems where the diffusion terms are discretized using Crouzeix-Raviart piecewise linear finite elements on a triangular grid and an upwind barycentric finite volumes for the convective terms. The time integration is carried out using an implicit Euler approach. In the area of solute transport problems, a proper orthogonal decomposition (POD) is combined with classical finite volume element method where an error estimate between the reduced-order POD and conventional FVE

ICCS Camera Ready Version 2024
To cite this paper please use the final published version:
DOI: 10.1007/978-3-031-63783-4_4

solutions is discussed [10]. In [8] the authors presented a discontinuous finite volume element discretization for a coupled Navier–Stokes Cahn–Hilliard phase field model. An analogous approach with mesh adaptivity is presented in [7] to solve the nonlinear Allen-Cahn equation in two-space dimensions, where backward Euler scheme is used for time integration and the nonlinearity is solved using Newton iterative method.
The aim of this work is to construct a new backward-characteristics finite volume element (BC-FVE) method able to accurately approximate stiff transport problems on unstructured grid. This is achieved by merging the advantages of a monotone backward characteristics method and a Petrov-Galerkin finite volume method. The novel method also avoids linearisation process of the convective terms. The accuracy of the new method is tested for stiff transport problems with analytical solution, including pollutant transport in the Loukkos river in northern Morocco. The results presented in this paper show high resolution of the proposed BC-FVE method in simulating transport and dispersion of pollutants on large sea-surface regions.

2 Monotone backward-characteristics scheme for the convective term

In this section, we construct an essentially non-oscillatory backward-characteristics scheme to solve highly convective problems. To this end, given a two-dimensional bounded domain $\Omega \subset \mathbb{R}^2$ with Lipschitz boundary Γ and a time interval $[0, T]$, we are interested in solving the following problem:

$$\begin{aligned} \frac{\partial c}{\partial t} + \mathbf{u}(t, \mathbf{x}, c) \cdot \nabla c = \nabla \cdot (\mathbf{K} \nabla c), \qquad (t, \mathbf{x}) \in (0, T) \times \Omega, \\ c(0, \mathbf{x}) = c_0(\mathbf{x}), \qquad \mathbf{x} \in \Omega. \end{aligned} \tag{1}$$

Here, $c(t, \mathbf{x})$ denotes the concentration of a species, $\mathbf{u}\,(t, \mathbf{x}, c)$ is the velocity field which may depend on the solution c, and $c_0(\mathbf{x})$ is a fixed initial condition. We assume that equation (1) is equipped with appropriate boundary conditions. The quantity $\mathbf{K}$ is the diffusivity tensor which is uniformly positive definite on Ω with components in $L^\infty(\Omega)$.
Consider the time interval $[t^n, t^{n+1}]$ and let $\Delta t = t^{n+1} - t^n$ denote the time step size. The spatial discretization of Ω consists of a quasi-uniform regular triangulation $\mathcal{T}_h$ consisting of triangular elements $\mathcal{K}_k$ such that $\Omega = \bigcup_{k=1}^{N} \mathcal{K}_k$ where N denotes the total number of triangles. We introduce a dual mesh $\mathcal{T}_h^*$ associated to $\mathcal{T}_h$ such that a given triangle $\mathcal{K}$ with vertices e_1, e_2 and e_3 is divided into six pieces by satisfying the following relations

$$\frac{|e_1 e_{1,2}^s|}{|e_1 e_2|} = \frac{|e_{2,1}^s e_2|}{|e_1 e_2|} = s, \quad \frac{|e_1 e_{1,2}^r|}{|e_1 \mathcal{E}_2|} = r, \quad \frac{|e_2 e_{2,3}^s|}{|e_2 e_3|} = \frac{|e_{3,2}^s e_3|}{|e_2 e_3|} = s, \quad \frac{|e_2 e_{2,3}^r|}{|e_2 \mathcal{E}_3|} = r,$$

$$\frac{|e_3 e_{3,1}^s|}{|e_3 e_1|} = \frac{|e_{1,3}^s e_1|}{|e_3 e_1|} = s, \quad \frac{|e_3 e_{3,1}^r|}{|e_3 \mathcal{E}_1|} = r,$$

ICCS Camera Ready Version 2024
To cite this paper please use the final published version:
DOI: 10.1007/978-3-031-63783-4_4

where $s \in (0, \frac{1}{2})$ and $r \in (0, \frac{2}{3})$ and $\mathcal{E}_j$ denotes the midpoint of the segment $e_i e_j$. By doing so, we obtain a partition of the triangle $\mathcal{K}$, which consists of three pentagons and three quadrilaterals as illustrated in Fig. 1. Our control volumes $\mathcal{D}_m$ are then polygons surrounding a vertex e_j or a midpoint $\mathcal{E}_j$. Therefore we obtain a family of control volumes covering the domain Ω with a total number n_v of control polygons $\mathcal{D}_m$. Solving the advected part of (1) using the method

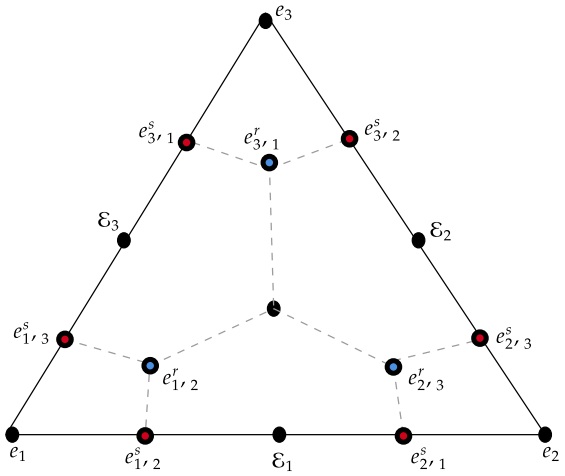

Fig. 1. A schematic diagram showing the partition of a triangle into three quadrilaterals and three pentagons.

of characteristics requires the solution of the following problem

$$\begin{aligned} \frac{d\boldsymbol{\mathcal{X}}_m(t)}{dt} &= \boldsymbol{u}_m\left(t, \boldsymbol{\mathcal{X}}_m(t), c_m\right), \qquad t \in [t_n, t_{n+1}], \\ \boldsymbol{\mathcal{X}}_m(t_{n+1}) &= \boldsymbol{x}_m, \end{aligned} \tag{2}$$

where $\boldsymbol{\mathcal{X}}_m(t) = (X_m(t), Y_m(t))^T$ denotes the departure point at time t of a particle that will arrive at the centroid $\boldsymbol{x}_m = (x_m, y_m)^T$ of the control volume $\mathcal{D}_m$ at time t_{n+1}. To solve problem (2) we use the well-known third-order Runge-Kutta scheme [6, Table II.1.1]. Next, integrating the transport equation $\frac{\partial c}{\partial t} + \mathbf{u} \cdot \nabla c = 0$ along the characteristic curves yields

$$c(t_{n+1}, \boldsymbol{x}_m) = c\left(t_n, \boldsymbol{\mathcal{X}}_m(t_n)\right). \tag{3}$$

In general, the departure points $\boldsymbol{\mathcal{X}}_m(t_n)$ do not lie on a mesh point. Therefore, an interpolation is required. This yields

$$c\left(t_n, \boldsymbol{\mathcal{X}}_m(t_n)\right) = \sum_{k \in \mathcal{N}} C_k^n \Psi_k(\boldsymbol{\mathcal{X}}_m(t_n)), \tag{4}$$

ICCS Camera Ready Version 2024
To cite this paper please use the final published version:
DOI: 10.1007/978-3-031-63783-4_4

where $\mathcal{N}$ refers to the number of contributed points during local interpolation, C_m^n denotes the known solution at the vertex $\boldsymbol{x}_m$ at time t^n and Ψ_m, $m = 1, \ldots, n_v$ is the basis function evaluated at the departure point $\boldsymbol{\mathcal{X}}_m(t_n)$. It should be stressed that high-order interpolation schemes might exhibit nonphysical oscillations, where the solution undergoes strong variations in general [1]. To deal with those undesirable behaviors, we propose a combination of low and high order interpolation schemes such that the interpolated value remain within the largest and the smallest values of the solution in a set of points surrounding the feet of the characteristics. Therefore, the low- and high-order solutions are computed, respectively using the well-known inverse distance weighted (IDW) [9] and the inverse multiquadric (IMQ) interpolations [13] where the corresponding basis functions ψ_k and Θ_l are given by the formulas

$$\psi_k(\boldsymbol{\mathcal{X}}_m(t_n)) = \frac{(1/d_{mk})^2}{\sum_{k=1}^{n_{vL}}(1/d_{mk})^2}, \quad \Theta_l(\boldsymbol{\mathcal{X}}_m(t_n)) = \frac{1}{\sqrt{1+(\epsilon d_{ml})^2}},$$

where ϵ denotes the shape parameter [11] and d_{mk} is the Euclidean distance between the departure point $\boldsymbol{\mathcal{X}}_m(t_n)$ to the point $\boldsymbol{x}_k$ calculated as

$$d_{mk} = \|\boldsymbol{\mathcal{X}}_m(t_n) - \boldsymbol{x}_k\| = \sqrt{\big(X_m(t_n) - x_k\big)^2 + \big(Y_m(t_n) - y_k\big)^2}.$$

See Fig. 2 for a graphical depiction. Thus, given the initial solution, the main steps used in the proposed BC-FVE to solve the advected part of problem (1) along a time step $[t^n, t^{n+1}]$ are summarized in Algorithm 1.

Algorithm 1 One time step of the BC-FVE approach for solving the advected part of problem (1).

1: Calculate the departure point $\boldsymbol{\mathcal{X}}_m(t_n)$.

2: Compute the high- and low-order solutions

$$c_{mH}^{n+1} = \sum_{l=1}^{n_{vH}} C_l^n \Theta_l(\boldsymbol{\mathcal{X}}_m^n) \text{ and } c_{mL}^{n+1} = \sum_{k=1}^{n_{vL}} C_k^n \psi_k(\boldsymbol{\mathcal{X}}_m^n).$$

3: Given the host control volume $\mathcal{D}_m^*$, compute

$$c^{\max} = \max(c_1^n, c_2^n, \ldots, c_{n_{vH}}^n) \text{ and } c^{\min} = \min(c_1^n, c_2^n, \ldots, c_{n_{vH}}^n).$$

4: Set

$$\alpha_m = \begin{cases} \min\Big(1, \frac{c^{\max} - c_{mL}^{n+1}}{c_{mH}^{n+1} - c_{mL}^{n+1}}\Big), & \text{if} \quad c_{mH}^{n+1} - c_{mL}^{n+1} > 0, \\ \min\Big(1, \frac{c^{\min} - c_{mL}^{n+1}}{c_{mH}^{n+1} - c_{mL}^{n+1}}\Big), & \text{if} \quad c_{mH}^{n+1} - c_{mL}^{n+1} < 0, \\ 0, & \text{if} \quad c_{mH}^{n+1} - c_{mL}^{n+1} = 0. \end{cases}$$

5: Update the solution as

$$c_m^{n+1} = c_{mL}^{n+1} + \alpha_m \left(c_{mH}^{n+1} - c_{mL}^{n+1}\right).$$

ICCS Camera Ready Version 2024
To cite this paper please use the final published version:
DOI: 10.1007/978-3-031-63783-4_4

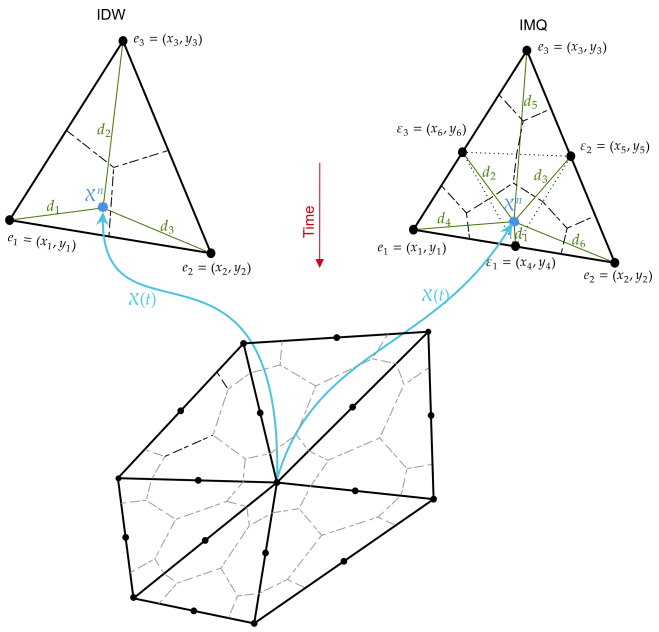

Fig. 2. A schematic diagram showing the main quantities used to interpolate the solution from the computed departure points. For low-order IDW interpolation $n_{vL} = 3$ whereas for high-order IMQ interpolation $n_{vH} = 6$.

3 Petrov-Galerkin finite volume scheme for the diffusive term

After dealing with the convective term, we are left with the following parabolic equation expressed in terms of the material derivative

$$\frac{Dc}{Dt} = \nabla \cdot (\mathbf{K} \nabla c). \tag{5}$$

The aim of this section is to descritize the diffusive term using the well-known Petrov-Galerkin finite volume method [15, 5]. Assuming the computational domain is discretized as described in section 2. In order to derive the weak form of problem (5), we consider the following finite element space for the primal mesh

$$\mathbb{V}(\mathcal{T}_h) := \left\{ w_h \in H_0^1(\Omega) \;\middle|\; w_h|_{\mathcal{K}_k} \in \mathcal{P}_2,\ \forall \mathcal{K}_k \in \mathcal{T}_h \right\},$$

where $\mathcal{P}_2$ denotes the piecewise quadratic polynomial space. We are given also a piecewise constant function space for the dual mesh

$$\mathbb{W}(\mathcal{T}_h^*) := \left\{ v_h \in L^2(\Omega) \;\middle|\; v_h|_{\mathcal{D}_m} \in \mathcal{P}_0,\ \forall \mathcal{D}_m \in \mathcal{T}_h^* \right\},$$

ICCS Camera Ready Version 2024
To cite this paper please use the final published version:
DOI: 10.1007/978-3-031-63783-4_4

where $\mathcal{P}_0$ denotes the constant polynomial space. Note that the spaces $\mathbb{V}(\mathcal{T}_h)$ and $\mathbb{W}(\mathcal{T}_h^*)$ are given by

$$\mathbb{V}(\mathcal{T}_h) = \text{span}\{\phi_l(\boldsymbol{x}),\ l = 1, \ldots, n_v\},\ \mathbb{W}(\mathcal{T}_h^*) = \text{span}\{\mathbb{1}_{\mathcal{D}_m}(\boldsymbol{x}),\ m = 1, \ldots, n_v\},$$

where ϕ_l denotes the standard quadratic Lagrange basis function and the characteristic function $\mathbb{1}_{\mathcal{D}_m}$ is defined over each control volume $\mathcal{D}_m$ as

$$\mathbb{1}_{\mathcal{D}_m}(\boldsymbol{x}) = \begin{cases} 1, & \text{if} \quad \boldsymbol{x} \in \mathcal{D}_m, \\ 0, & \text{elsewhere.} \end{cases}$$

The discrete balance equation associated to problem (5) is given by integrating the whole equation over each control volume $\mathcal{D}_m$ and using the divergence theorem to obtain

$$\int_{\mathcal{D}_m} \frac{Dc_h}{Dt} dV = -\int_{\partial\mathcal{D}_m} (\mathbf{K}\nabla c_h) \cdot \mathbf{n}_e d\sigma, \tag{6}$$

where $\mathbf{n}_e$ denotes the outward normal vector to the edge e of $\mathcal{D}_m$. Applying the BDF2 scheme yields

$$\int_{\mathcal{D}_m} \left(\frac{3}{2\Delta t} c_h^{n+1}(\boldsymbol{x}) - \frac{2}{\Delta t} c_h^n(\boldsymbol{\mathcal{X}^n}(\boldsymbol{x})) - \frac{1}{2\Delta t} c_h^{n-1}(\boldsymbol{\mathcal{X}^{n-1}}(\boldsymbol{x})) \right) dV = \tag{7}$$
$$-\int_{\partial\mathcal{D}_m} (\mathbf{K}\nabla c_h^{n+1}(\boldsymbol{x})) \cdot \mathbf{n}_e d\sigma,$$

where $\mathcal{X}^n(\boldsymbol{x})$ and $\mathcal{X}^{n-1}(\boldsymbol{x})$ denote the departure points at times t_n and t_{n-1} respectively, of the particle that will reach the point $\boldsymbol{x}$ at time t_{n+1}. Therefore, c_h^n is the solution evaluated using the backward-characteristics method at t^n, and c_h^{n-1} is the solution evaluated two time steps back along the characteristics. To construct a finite volume element scheme, we are seeking for a solution $c_h \in \mathbb{V}(\mathcal{T}_h)$ as in the framework of finite element analysis. Taking into consideration that the semi-discrete solution c_h can be rewritten in terms of the chosen basis functions as

$$c_h^n(\boldsymbol{x}) = \sum_{l=1}^{n_v} C_l^n \phi_l(\boldsymbol{x}),\ m = 1, \ldots, n_v.$$

Inserting the above expression into (7) and rearranging all terms yields the following compact form

$$\frac{3}{2\Delta t}\mathbf{M}C^{n+1} + \mathbf{S}C^{n+1} = \frac{2}{\Delta t}\tilde{\mathbf{H}}^n - \frac{1}{2\Delta t}\hat{\mathbf{H}}^{n-1}, \tag{8}$$

where $\mathbf{M}$ and $\mathbf{S}$ are the mass and stiffness matrices which entries are given by

$$M_{ml} = \int_\Omega \phi_l(\boldsymbol{x}) \mathbb{1}_{\mathcal{D}_m}(\boldsymbol{x}) dV, \qquad S_{ml} = -\int_{\partial\mathcal{D}_m} (\mathbf{K}\nabla\phi_l(\boldsymbol{x})) \cdot \mathbf{n}_e(\boldsymbol{x}) d\sigma.$$

ICCS Camera Ready Version 2024
To cite this paper please use the final published version:
DOI: 10.1007/978-3-031-63783-4_4

The right-hand sides $\tilde{\mathbf{H}}^n$ and $\hat{\mathbf{H}}^{n-1}$ are given by the following formulas, where the corresponding integral are approximated using the Gauss-Legendre quadrature rule

$$\tilde{\mathbf{H}}^n := \left(\int_\Omega \mathbf{c_h^n}(\mathcal{X}^{\mathbf{n}}(\boldsymbol{x}))\phi_l(\boldsymbol{x})\mathbb{1}_{\mathcal{D}_m} dV \right), \ \hat{\mathbf{H}}^{n-1} := \left(\int_\Omega \mathbf{c_h^{n-1}}(\mathcal{X}^{\mathbf{n-1}}(\boldsymbol{x}))\phi_l(\boldsymbol{x})\mathbb{1}_{\mathcal{D}_m} dV \right).$$

4 Numerical results

In this section, we examine the accuracy of the novel BC-FVE on several benchmark of transport problems including a system of nonlinear Burgers equations and transport of a pollutant in coastal areas.

4.1 Slotted cylinder

Our first test is the slotted cylinder. The rotation is driven by $\mathbf{u}(x, y) = (-4y, 4x)^T$ and the diffusive term is taken as zero. For a given (x_0, y_0), let $\rho(x, y) = \sqrt{(x - x_0)^2 + (y - y_0)^2}$. The slotted cylinder is defined as

$$c(0, x, y) = \begin{cases} 4, & \text{if} \quad \rho(x, y) \leq 1 \quad \text{and} \quad (\ |x - x_0| \geq 0.03 \quad \text{or} \quad y \geq 0.22), \\ 0, & \text{elsewhere.} \end{cases}$$

This problem has served as a prototype to examine the performance of several

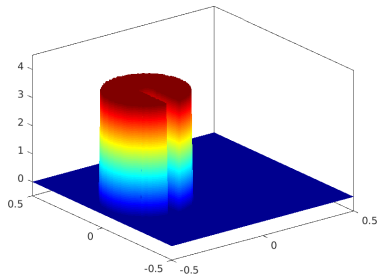

Fig. 3. 3D representation of the initial solution of slotted cylinder. The minimum of c is 0 and its maximum is 4.

algorithms for flow transport. The snap-shot of analytical solution in Fig. 3 is used to quantify the accuracy of the novel method. The computational domain is partitioned into 6274 control volumes. In Fig. 4, we display the obtained numerical solutions, for low-order interpolation, high-order interpolation and limiting approach, for CFL = 10.5. The numerical solutions after one revolution (first column) are then repeated but after four revolutions, as illustrated in the second column. The clear indication from Fig. 4 that the IDW solution

ICCS Camera Ready Version 2024
To cite this paper please use the final published version:
DOI: 10.1007/978-3-031-63783-4_4

is dissipative and substantially greater distortion appears after four revolutions. On the other side, the IMQ solution exhibits steep gradients which become more steep after four revolutions. However, all the non desirable effects are suppressed when merging the two interpolations and the BC-FVE solution results in a more accurate solution where the slotted cylinder shape is well reproduced during time evolution. To further quantify the accuracy of the proposed approach and analyze the effect of CFl on the stability of the method, we list in Fig. 5 the cross-sections along $y = 0$ after one and four revolutions for different values of CFL number. The corresponding cross-sections of the analytical solution are added for comparison reasons. It is known that backward characteristics methods work with high precision for large CFL numbers. Indeed, for CFL $= 0.87$ both IDW and IMQ solutions exhibit nonphysical oscillations. Unfortunately, the BC-FVE solution is also less accurate for same value of CFL. However, the more the CFL number is high the more accurate results we obtain. Indeed, an intriguing finding is that the inaccuracy of backward characteristics schemes decreases as the time step increases in a certain range of parameters.

4.2 Viscous Burgers equations

In the second test we are concerned with a system of nonlinear Burgers' equations given as

$$\frac{\partial \boldsymbol{u}}{\partial t} + \boldsymbol{u} \cdot \nabla \boldsymbol{u} - \frac{1}{Re} \Delta \boldsymbol{u} = \boldsymbol{0}, \tag{9}$$

where $\boldsymbol{u} = (u, v)^\top$ is the velocity field, u the velocity in x-direction, v the velocity in y-direction, and Re is the Reynolds number. The computational domain is the square domain $\Omega = [-2, 2] \times [-2, 2]$. Initial and boundary conditions are chosen to satisfy the following analytical solution

$$u(t, x, y) = v(t, x, y) = \frac{1}{2} \left(1 - \tanh \left(\frac{Re}{4} (x + y - t) \right) \right),$$

In table 1 we summarize the minimum (Min), the maximum (Max) of the velocity component u, the L^2-error, the rate of convergence and the computational cost (CPU) obtained for the IDW scheme, the IMQ scheme and the novel BC-FVE for two values of Reynold number Re. It should be noted that the Min and the Max results are taken in the range of large gradients. Roughly speaking, better accuracy is achieved for $Re = 10^4$. In addition, the IMQ solution produces more accurate convergence rates even though the solution is not monotone. on the other side, the IDW solution is very dissipative. The results sound more accurate when merging both interpolation and the BC-FVE solution is monotone where the convergence rates are clearly improved. In term of computational costs, the CPU time required for the IDW solution is about 3/4 times the CPU time required for the IMQ solution. The BC-FVE solution in tern, is about 5/3 times the IMQ solution.

ICCS Camera Ready Version 2024
To cite this paper please use the final published version:
DOI: 10.1007/978-3-031-63783-4_4

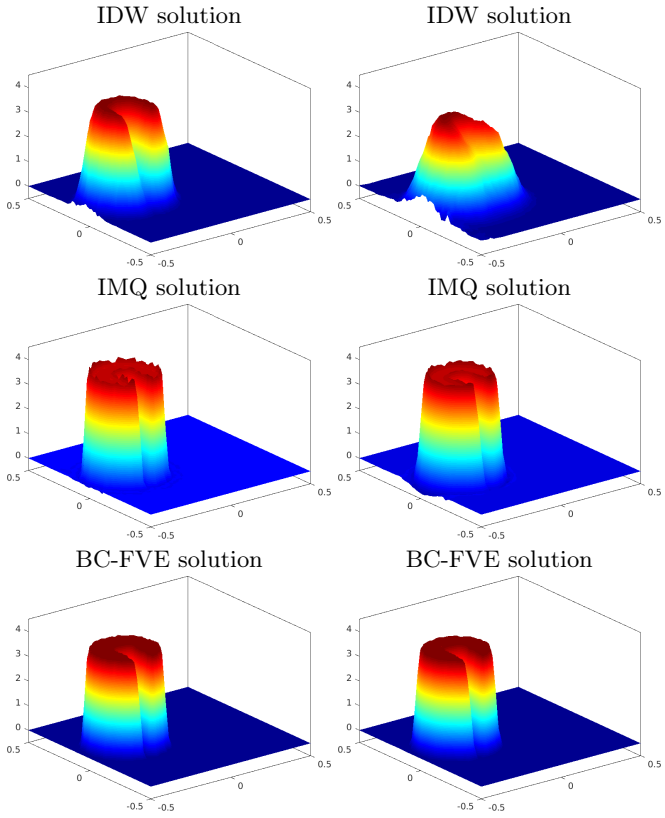

Fig. 4. Snapshots for Example 4.1 obtained using different methods after one revolution (first colomn) and four revolutions (second colomn).

4.3 Transport in the Loukkos river in northern Morocco

In the last example we turn our attention to a real application over the physical domain given in Fig. 6, where we consider the transport of some sediments concentration c in the Loukkos river in the northern Morocco. The Loukkos river is one of the largest streams in Morocco with an average flow of 50 m^3/s. The river flows in the Atlantic Ocean and plays an important role in preserving the biodiversity, containing one of the most fertile and productive agricultural lands in the country.
The main objective in this study is to analyze the performance of the new BC-FVE method to handle complex geometries in coastal zones for long-term simulations. Therefore, we address the solution to the transport equation (1) within the computational domain defined by the Loukkos river and Larache coastal zone as illustrated in Fig. 7. An incompressible Navier-Stokes code implemented in FEniCS software is used to generate the velocity field and the results are depicted in

ICCS Camera Ready Version 2024
To cite this paper please use the final published version:
DOI: 10.1007/978-3-031-63783-4_4

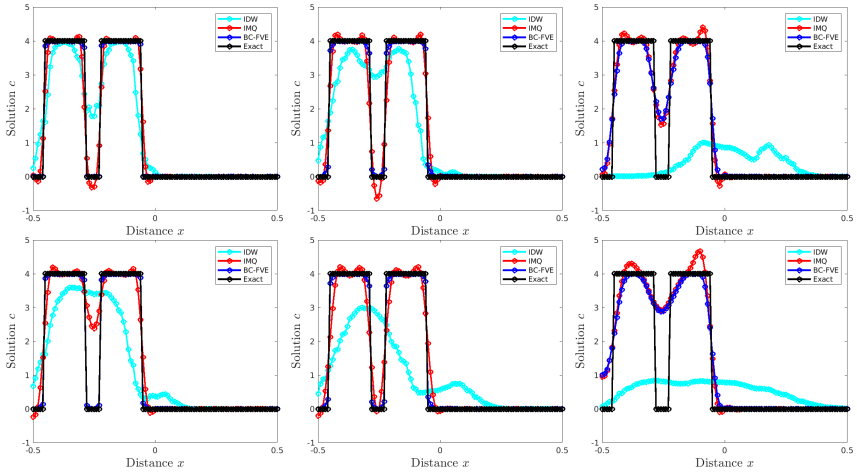

Fig. 5. Cross sections along $y = 0$. From left to right: CFL = 10.5, CFL = 4.63, CFL = 0.87. First row: 1 revolution. Second row: 4 revolutions.

Table 1. Computational results for Example 4.2 at time $t = 1$ obtained as a comparative study between the three discussed methods. The CPU times are given in seconds.

		$Re = 10^4$					$Re = 20$				
	n_v	Min(u)	Max(u)	L^2-error	Rate	CPU	Min(u)	Max(u)	L^2-error	Rate	CPU
IDW	257	1.452E-10	0.851	3.023E-01	—	1.18	2.929E-02	0.817	3.518E-01	—	1.38
	622	3.294E-14	0.884	1.898E-01	0.67	3.14	5.403E-18	0.870	1.986E-01	0.82	3.73
	1422	6.233E-16	0.894	9.421E-02	1.01	11.1	1.120E-57	0.891	8.986E-02	1.14	12.1
	2945	9.638E-18	0.938	4.331E-02	1.12	47.5	1.213E-17	0.914	3.986E-02	1.17	64.3
IMQ	257	1.452E-10	1.042	2.953E-02	—	1.58	-1.052E-03	1.432	1.946E-01	—	1.85
	622	1.144E-14	1.034	5.862E-03	2.33	4.17	-1.345E-03	1.303	4.953E-02	1.97	4.96
	1422	4.400E-15	1.026	1.101E-03	2.41	15.0	-1.293E-03	1.217	1.196E-02	2.05	16.3
	2945	1.213E-17	1.019	2.213E-04	2.31	63.2	1.213E-17	1.135	2.696E-03	2.14	85.6
BC-FVE	257	2.442E-27	0.998	2.942E-02	—	2.63	2.752E-16	0.999	1.836E-01	—	3.06
	622	3.534E-30	1.000	5.712E-03	2.36	6.95	1.425E-19	1.000	4.986E-02	1.88	8.27
	1422	4.218E-32	1.000	1.173E-03	2.28	25.2	1.293E-23	1.000	1.011E-02	2.30	27.3
	2945	1.423E-33	1.000	2.305E-04	2.34	105	1.003E-23	1.000	2.381E-03	2.08	144

Fig. 7. The problem model is subject to given inflow conditions $\mathbf{u}_\infty = 0.65\ m/s$ on the river entrance, nonslip condition on land boundaries, while the ocean boundaries remains free. The problem assumes a kinematic viscosity of 10 m^2/s and is subject to a release defined by a source term specified as follows:

$$f(x, y, t) = \exp\left(-\frac{(x - x_r)^2 + (y - y_r)^2}{\sigma^2}\right), \tag{10}$$

where $\sigma = 0.2\ km$ and $(x_r, y_r) = (4.69\ km, 0.15\ km)$ is the selected location for concentration release, see the release point R in Fig. 6. In our simulations, an unstructured triangular mesh with 5036 nodes for low order method and 19282

ICCS Camera Ready Version 2024
To cite this paper please use the final published version:
DOI: 10.1007/978-3-031-63783-4_4

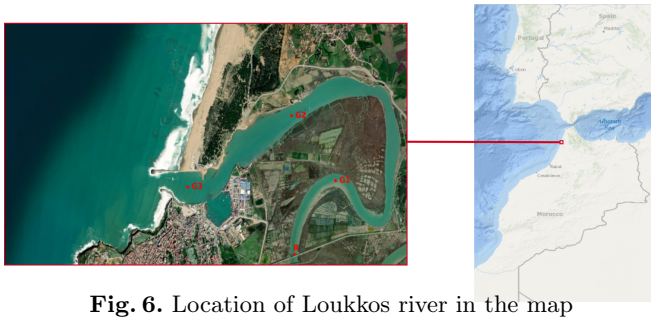

Fig. 6. Location of Loukkos river in the map

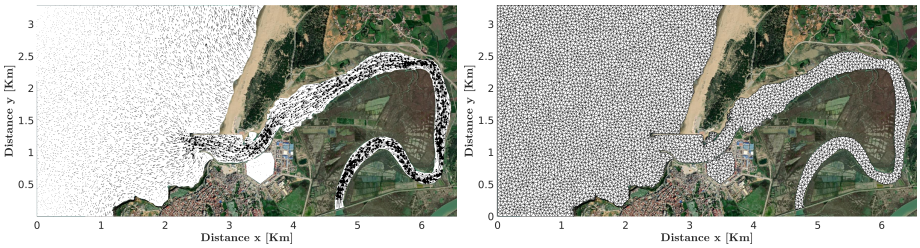

Fig. 7. Velocity field (left), computational domain and location of gauges (right).

nodes for high order method, are used. In Fig. 8 we present the simulation of the concentration c at six distinct times: t = 25 min, 2 hours, 4 hours, 6 hours, 8 hours, and 10 hours. In the early stages of the simulation, the concentration fronts released in the river begins to evolve until it flows into the Atlantic Ocean. Henceforth, the advection of the sediment c into the ocean eventually condensates in the bay before it stagnates within it, forming large spot in the exit of the river. It should be stressed that despite the challenges posed by the complex geometry and the flow features, the novel BC-FVE method demonstrates high performance in capturing high gradients within the advancing plume. It is crucial to note that unlike prior cases, in which convection-diffusion problems were treated in basic geometries with known velocity fields, the current problem is addressed within a wide area with irregular geometry and complex flow patterns. To further quantify the accuracy of the method with a reference solution, we monitor the concentration at three gauges, G1, G2, and G3, situated in the river at (5.36 km, 1.16 km), (4.64 km, 2.05 km), and 2.94 km, 1.07 km), respectively, as illustrated in Fig. 6. Keeping the same mesh resolution as before, we list in Fig. 9 the time evolution of the concentration at the given gauges at time t = 12 hours. Note that the reference solution is computed on a reference mesh with 49429 elements and 100349 nodes. The clear indication from Fig. 9 is that the IMQ solution exhibits again oscillations and clearly steep layers appear in the regions of large gradients (compare Fig. 9 G 3). This is potentially attributed to complex feature of the bended geometry nearby G 1. From the same plot,

ICCS Camera Ready Version 2024
To cite this paper please use the final published version:
DOI: 10.1007/978-3-031-63783-4_4

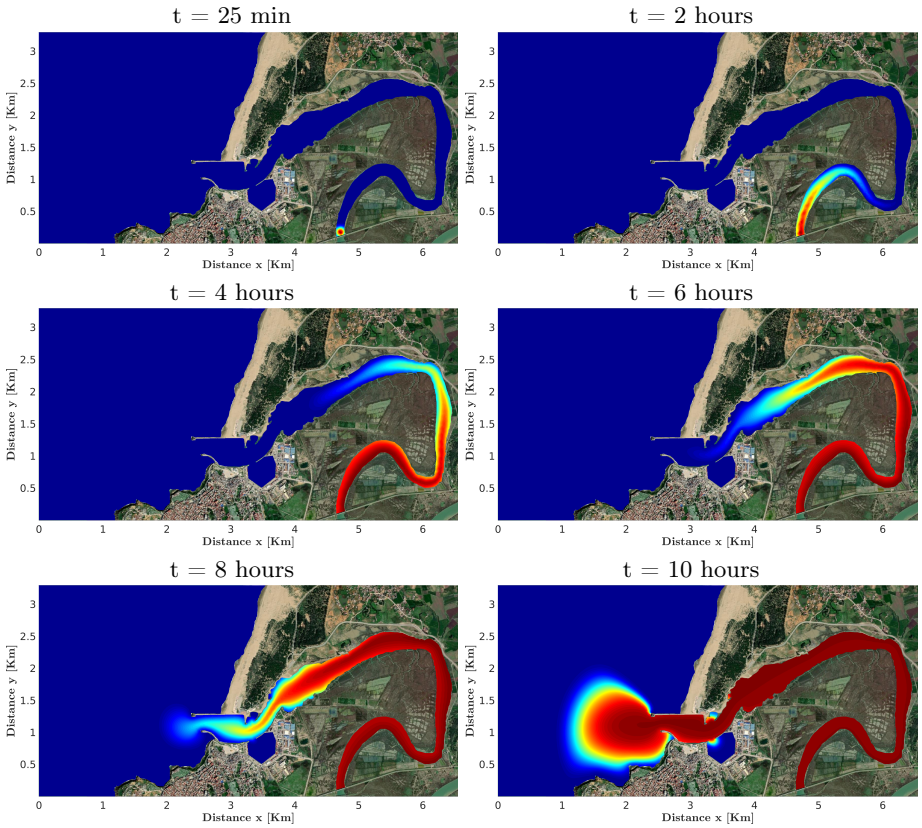

Fig. 8. Concentration snapshots for the transport problem in the Loukkos river using the proposed backward Petrov-Galerkin finite volume method (BC-FVE).

the IDW solution exhibits numerical diffusion. By its turn, the BC-FVE solution results in a stable and monotone behavior in the selected gauges during time evolution. Moreover, a quantitative study confirms that the novel BC-FVE method results are in good agreement with the reference solution.

5 Conclusions

In this work we have presented a novel backward-characteristics finite volume element method for solving a class of convection-dominated diffusion problems. The outcoming features of this method is to preserve the monotonicity and accuracy of the solution with the minimum possible of computational cost. This is achieved by the virtue of backward-characteristics scheme where low and high order interpolation techniques are both used to balance the characteristics of the solution during time evolution. Indeed, the interpolated value remains within the largest and the smallest values of the solution in a set of points surrounding the

ICCS Camera Ready Version 2024
To cite this paper please use the final published version:
DOI: 10.1007/978-3-031-63783-4_4

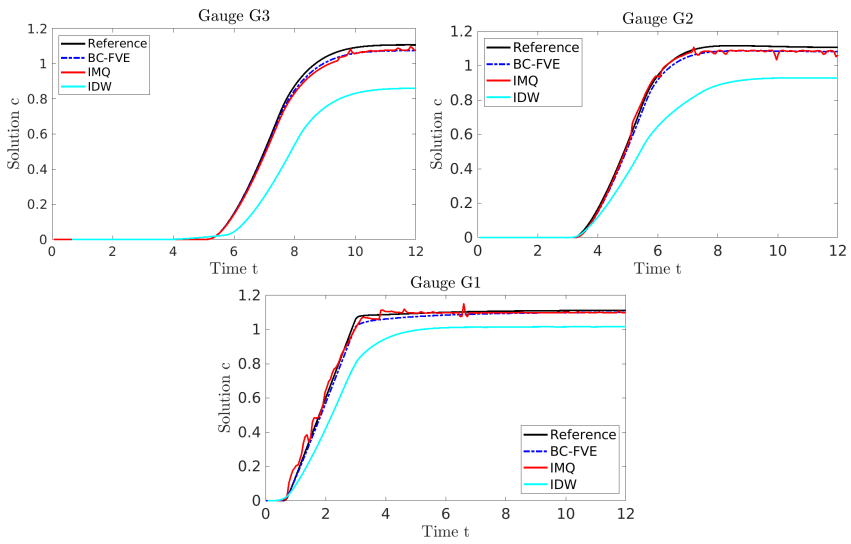

Fig. 9. Time evolution of c in the selected three gauges for the transport of a pollutant in the Loukkos river.

feet of the characteristics. The diffusive term is approximated with a Petrov-Galerkin finite volume scheme where a finite partitioning set of control volumes is used to discretize the equation and a restriction of admissible functions of finite element space are used to discretize the solution. The obtained results demonstrate the ability of the new algorithm to accurately maintain the shape of the computed solutions in the presence of sharp gradients and shocks. **Future work will focus on the one hand, on extending the current approach to coupled flow-transport, where the flow is modeled by the incompressible Navier-Stokes equations. On the other hand, we aim to explore the time adaptation and construct an efficient adaptive BDF2 along the characteristics in order to minimize the computational cost.**

References

1. R. Bermejo. Analysis of a class of quasi-monotone and conservative semi-lagrangian advection schemes. *Numerische Mathematik*, 87(4):597–623, 2001.
2. N. Crouseilles, M. Mehrenberger, and E. Sonnendrücker. Conservative semi-Lagrangian schemes for Vlasov equations. *Journal of Computational Physics*, 229(6):1927–1953, 2010.
3. B. Després. Polynomials with bounds and numerical approximation. *Numerical Algorithms*, 76:829–859, 2017.
4. P. Deuring and M. Mildner. Stability of a combined finite element-finite volume discretization of convection-diffusion equations. *Numerical Methods for Partial Differential Equations*, 28(2):402–424, 2012.

ICCS Camera Ready Version 2024
To cite this paper please use the final published version:
DOI: 10.1007/978-3-031-63783-4_4

5. M. Feistauer, J. Felcman, M. Lukácová-Medvid'ová, and G. Warnecke. Error estimates for a combined finite volume-finite element method for nonlinear convection–diffusion problems. *SIAM Journal on Numerical Analysis*, 36(5):1528–1548, 1999.
6. E. Hairer, S.P. Nørsett, and G. Wanner. *Solving ordinary differential equations I.* Springer, Berlin, 2 edition, 1993.
7. J. Li, J. Zeng, and R. Li. An adaptive discontinuous finite volume element method for the Allen–Cahn equation. *Advances in Computational Mathematics*, 49(4):55, 2023.
8. R. Li, Y. Gao, J. Chen, L. Zhang, X. He, and Z. Chen. Discontinuous finite volume element method for a coupled Navier–Stokes–Cahn–Hilliard phase field model. *Advances in Computational Mathematics*, 46:1–35, 2020.
9. G.Y. Lu and D.W. Wong. An adaptive inverse-distance weighting spatial interpolation technique. *Computers & Geosciences*, 34(9):1044–1055, 2008.
10. Z. Luo, H. Li, P. Sun, J. An, and I.M. Navon. A reduced-order finite volume element formulation based on POD method and numerical simulation for two-dimensional solute transport problems. *Mathematics and Computers in Simulation*, 89:50–68, 2013.
11. Michael Mongillo et al. Choosing basis functions and shape parameters for radial basis function methods. *SIAM undergraduate research online*, 4(190-209):2–6, 2011.
12. J.M. Qiu and C.W. Shu. Conservative semi-Lagrangian finite difference WENO formulations with applications to the Vlasov equation. *Communications in Computational Physics*, 10(4):979–1000, 2011.
13. S.A. Sarra and E.J. Kansa. Multiquadric radial basis function approximation methods for the numerical solution of partial differential equations. *Advances in Computational Mechanics*, 2(2):220, 2009.
14. T. Xiong, J.M. Qiu, Z. Xu, and A. Christlieb. High order maximum principle preserving semi-Lagrangian finite difference WENO schemes for the Vlasov equation. *Journal of Computational Physics*, 273:618–639, 2014.
15. Y. Zhou and J. Wu. A unified analysis of a class of quadratic finite volume element schemes on triangular meshes. *Advances in Computational Mathematics*, 46:1–31, 2020.

ICCS Camera Ready Version 2024
To cite this paper please use the final published version:
DOI: 10.1007/978-3-031-63783-4_4